Multimode character of quantum states released from a superconducting cavity

Maryam Khanahmadi [1,*] Mads Middelhede Lund [2] Klaus Mølmer,[3] and Göran Johansson[1,†]

[1]*Department of Microtechnology and Nanoscience, Chalmers University of Technology, 412 96 Gothenburg, Sweden*
[2]*Center for Complex Quantum Systems, Department of Physics and Astronomy, Aarhus University, 8000 Aarhus C, Denmark*
[3]*Niels Bohr Institute, University of Copenhagen, Blegdamsvej 17, DK-2100 Copenhagen, Denmark*

Quantum state transfer by propagating wave packets of electromagnetic radiation requires tunable couplings between the sending and receiving quantum systems and the propagation channel or waveguide. The highest fidelity of state transfer in experimental demonstrations so far has been in superconducting circuits. Here, the tunability always comes together with nonlinear interactions, arising from the same Josephson junctions that enable the tunability. The resulting nonlinear dynamics correlates the photon number and spatiotemporal degrees of freedom and leads to a multimode output state, for any multiphoton state. In this work, we study as a generic example the release of complex quantum states from a superconducting resonator, employing a flux tunable coupler to engineer and control the release process. We quantify the multimode character of the output state and discuss how to optimize the fidelity of a quantum state transfer process with this in mind.

I. INTRODUCTION

The exchange of quantum states between distant locations is an important ingredient in secure communication networks and in scalable architectures for quantum computing [1,2].

Quantum bits encoded in the higher dimensional oscillator modes of superconducting cavities have been demonstrated to withstand photon losses and permit elementary error correction [3–8]. It would be desirable to use such multiphoton quantum states also for quantum communication purposes [9,10].

While a linear mapping between a single oscillator mode and the continuum of propagating field modes, in principle, transfers the quantum state of the former to a traveling single-mode pulse, the temporal control of the release process is not trivial. In superconducting circuits, tunable couplers based on Josephson junctions are employed to control the evolution and release process in different architectures, such as fixed-frequency transmons, flux tunable transmons, or tunable transmission line resonators [11–20]. While the nonlinearity of the Josephson junction enables tunable coupling, it also adds effective self-Kerr and cross-Kerr terms to the oscillator Hamiltonian. These nonlinear terms may entangle the spatiotemporal release with the photon number contents of the pulse, and thus the emission becomes multimode in character and it may not function properly in a quantum network.

In this article, we present a general analysis that takes the multi-mode character of the emission process fully into account. We employ a master equation approach that readily incorporates both the coherent coupling to the output field and decay and decoherence channels, and we use the quantum regression theorem to assess the mode decomposition of the emitted radiation.

For the more quantitative discussion, we consider superconducting circuits. With low loss rates and strong coupling, these are promising platforms to efficiently prepare and emit quantum states into propagating modes [21,22]. Different studies and experiments have been done with a low number of photons [13,23]. In this paper, we theoretically analyze an experimentally relevant superconducting circuit architecture for which we can control the out-coupling strength and compute the accompanying nonlinear couplings. The propagation transfer and the recapture of the field by downstream circuit components can then be analyzed by the method presented in [24].

The article is structured as follows: In Sec. II, we provide the formalism determining the characteristics of the output field of the quantum system. In Sec. III, we describe the superconducting emitter and tunable out-coupler in detail, in Sec. IV we provide numerical results and study the quantitative effects of the nonlinearity on the multimode character of different bosonic quantum states released from the circuit, and in Sec. V, we characterize the quantum state of the most populated mode and optimize the drive on the system to encode our desired quantum state into that mode. Finally, we summarize the paper in Sec. VI.

II. MULTIMODE THEORY

To assess the consequence of emitting a field from a nonlinear system, we consider a single nonlinear resonator as a

---

*m.khanahmadi@chalmers.se
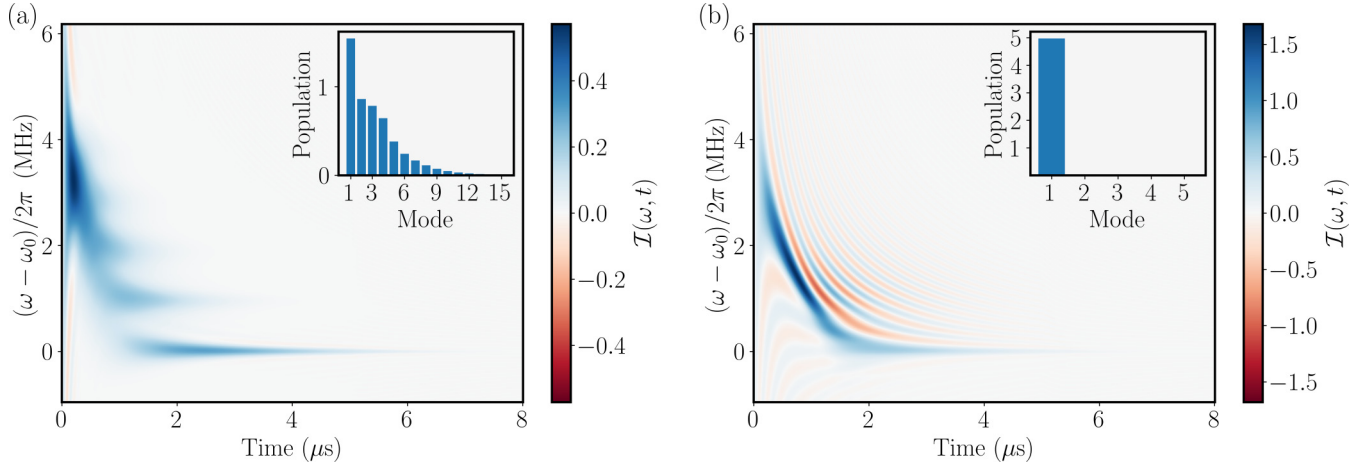†goran.l.johansson@chalmers.se

FIG. 1. Time-dependent spectra of the output field from a nonlinear (a) and a linear (b) resonator. Panel (a) shows the radiation from a non-linear resonator with constant frequency ω_0, outcoupling rate $1/\kappa = 1\,\mu s$, and Kerr coefficient $\chi/2\pi = 0.47\,\text{MHz}$ prepared in an initial Fock state $|n\rangle = |5\rangle$. The inset in panel (a) shows that the emitted radiation occupies several eigenmodes. In panel (b) we assume a vanishing Kerr coefficient $\chi = 0$ and a time-dependent oscillator frequency $\omega(t) = \omega_0 + \max(0, 2\chi[n\exp(-\kappa t) - 1])$. As shown in the inset of panel (b), the output field is a single-mode Fock state with $n = 5$.

toy model for a nonlinear emitter with the Hamiltonian

$$H_S(t) = \omega(t)a^\dagger a + \chi(t)a^{\dagger 2}a^2, \tag{1}$$

having time-dependent frequency $\omega(t)$ and self-Kerr coefficient $\chi(t)$, using angular frequency units of energy ($\hbar = 1$). If we assume the emitter is coupled to a waveguide with constant strength $\sqrt{\kappa}$, the evolution of the reduced density matrix $\varrho(t)$ of the resonator is described by the Lindblad master equation with a single Lindblad operator $\sqrt{\kappa}a$, describing the dissipation to the waveguide,

$$\frac{\partial \varrho(t)}{\partial t} = -i[H_S(t), \varrho(t)] + \kappa\left(a\varrho(t)a^\dagger - \frac{1}{2}\{a^\dagger a, \varrho(t)\}\right). \tag{2}$$

The expectation value and higher order correlation functions of the field leaking from the cavity are given by the equivalent expectation value and correlation functions of the intracavity (Heisenberg picture) field operators $\sqrt{\kappa}a^\dagger(t)$ and $\sqrt{\kappa}a(t)$. Of particular importance is the first-order, two-time autocorrelation function $\mathcal{G}^{(1)}(t_1, t_2) = \kappa\langle a^\dagger(t_2)a(t_1)\rangle$, as it permits expansion on an orthogonal set of temporal modes $v_i(t)$,

$$\mathcal{G}^{(1)}(t_1, t_2) = \sum_i n_i v_i^*(t_1)v_i(t_2), \tag{3}$$

with mean photon occupation number n_i. This procedure which is also applied to noisy classical signals is known as the Karhunen-Loève expansion and it has been extensively used in quantum optics; see [25]. The autocorrelation function $\mathcal{G}^{(1)}(t_1, t_2)$ can be calculated using the quantum regression theorem [26,27]

$$\mathcal{G}^{(1)}(t_1, t_2) = \kappa\text{Tr}[a^\dagger\mathcal{L}(t_2, t_1)[a\mathcal{L}(t_1, 0)\varrho_s(0)]], \tag{4}$$

where $\mathcal{L}(t', t)$ represents the linear time evolution map of the master equation (2) from time t to t'. We shall use the mode decomposition (3) to identify the most populated output mode of the cavity and subsequently determine the quantum state occupying this particular mode.

The time-dependent spectrum related to the autocorrelation function in Eq. (4) is found by the Fourier transform

$$\mathcal{I}(\omega, t) = \int_{-\infty}^{+\infty} ds\, \mathcal{G}^{(1)}\left(t + \frac{s}{2}, t - \frac{s}{2}\right) e^{-i\omega s}, \tag{5}$$

which provides information about the time-dependent frequency content of the output field.

Output field spectra for a nonlinear resonator and a linear resonator are shown in Fig. 1, where in both cases the resonator is initialized in the Fock state $|\psi\rangle = |5\rangle$. For the parameters in the figure caption, the time-dependent spectra show the emission of a wide range of frequencies for both linear and nonlinear resonators. The spectrum in Fig. 1(a) shows a visible gap between the frequency pertaining to each emitted photon, proportional to the amount of the Kerr nonlinearity 2χ. The inset shows that multiple output field modes are populated in the field emitted by the nonlinear resonator.

For comparison, in Fig. 1(b), we assume a linear resonator, $\chi = 0$, with a time-dependent frequency $\omega(t)$ chosen to give a similar frequency range of the emitted field as in (a). The inset in panel (b) shows that the output field in this case only occupies a single (chirped) mode. In the next section, we model a realistic quantum emitter implemented in superconducting circuits and we assess how the nonlinear elements used for tuning the emission process affect the mode character and purity of the emitted quantum state.

III. PHYSICAL MODEL

Several approaches have been used to map a stationary resonator mode to a propagating pulse mode. To optimally control the release of a quantum state, we consider the storage system (cavity), initiated in the desired quantum state $|\psi\rangle$, described by the creation and annihilation operators $a^\dagger$, a and frequency ω_a. The storage cavity is dispersively coupled to a flux-tunable transmon [22,28–30] described by the oper-
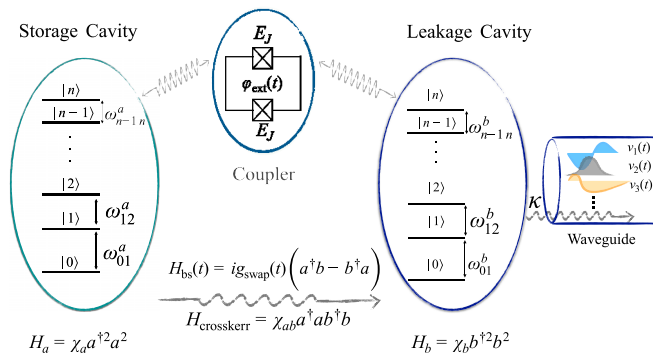
FIG. 2. Schematic of the emitter. The nonlinear coupler interacts with both the storage and the leakage cavity. By driving the coupler at the frequency $\omega_{01}^a - \omega_{01}^b$, it implements a frequency conversion and resonant transfer of quanta between the storage and leakage cavity, as governed by a beam splitter interaction $H_{bs}(t)$ between the two cavities at frequencies ω_{01}^a and ω_{01}^b. Due to the nonlinearity of the coupler, the beam splitter interaction is accompanied by self-Kerr and cross-Kerr nonlinear interactions; see Eq. (10), which leads to an output field populating several modes $v_1(t), v_2(t), v_3(t), \ldots$.

ators $c^\dagger$, c and frequency ω_c, through the coupling strength $g_{ac} \ll |\omega_c - \omega_a|$. In addition to the storage cavity, the coupler is also dispersively coupled to a leakage cavity, described by frequency ω_b and operators $b^\dagger$, b, with the coupling $g_{bc} \ll |\omega_b - \omega_c|$; see Fig. 2.

The entire system is described by the effective Hamiltonian

$$
\begin{aligned}
H_S(t) = {} & \omega_a a^\dagger a + \omega_b b^\dagger b + \omega_c c^\dagger c \\
& + 2E_J \left[\cos\left(\frac{\varphi_{ext}(t)}{2}\right) - \cos\left(\frac{\varphi_{dc}}{2}\right) \right] \frac{\varphi_c^2}{2} \\
& - 2E_J \cos\left(\frac{\varphi_{ext}(t)}{2}\right) \frac{\varphi_c^4}{4!},
\end{aligned} \quad (6)
$$

where φ_c and E_J correspond to the reduced flux operator of the transmon and the energy of the junction, respectively. The AC flux drive on the coupler is $\varphi_{ext}(t) = \varphi_{dc} + F(t)\sin(\omega_d t)$ which is described by the time-dependent amplitude $F(t) \equiv \delta \tanh(t/t_0) \ll 1$ and frequency ω_d, where δ and t_0 correspond to the amplitude and duration of turning on the drive, respectively. For more details on the derivation of the Hamiltonian (6) see Appendix A.

In the dispersive regime, the reduced flux of the coupler is found as the superposition of all dressed modes [31,32]

$$
\varphi_c = \frac{2\pi}{\phi_0} \phi_c,
$$

$$
\phi_c = \frac{\lambda_a(a + a^\dagger) + \lambda_b(b + b^\dagger) + \lambda_c(c + c^\dagger)}{\sqrt{2}} \equiv \frac{A + A^\dagger}{\sqrt{2}}, \quad (7)
$$

where ϕ_c is the flux of the coupler and the coefficients $\lambda_{a,b,c}$ are described in Eq. (A18). Using the Taylor expansion (A10), we insert Eq. (7) in the Hamiltonian (6), thus the second line

of Eq. (6) is obtained as

$$
\begin{aligned}
H^l(t) = {} & \frac{-2E_J\pi^2}{\phi_0^2} \left[\frac{\sin\left(\frac{\varphi_{dc}}{2}\right) F(t)\sin(\omega_d t)}{2} \right. \\
& \left. + \frac{\cos\left(\frac{\varphi_{dc}}{2}\right)}{8} F(t)^2 \sin(\omega_d t)^2 \right] (2A^\dagger A + \bar\lambda), \quad (8)
\end{aligned}
$$

where $\bar\lambda = [A, A^\dagger]$. The third line of Eq. (6) (fourth order of the flux operator), provides the nonlinear interactions as follows:

$$
H_{nl} \approx \frac{-\pi^4 E_J \cos\left(\frac{\varphi_{ext}(t)}{2}\right)}{3\phi_0^4} [12\bar\lambda A^\dagger A + 6A^\dagger A^\dagger AA], \quad (9)
$$

where we keep only the terms conserving the number of quanta.

We assume that the coupler is initiated in the ground state and mediates the resonant frequency conversion without itself being excited. This permits the elimination of its quantum degrees of freedom at all times. If we consider $\omega_d = \omega_b - \omega_a$ and utilize the rotating wave approximation and transform to the rotating frame interaction picture with respect to $\omega_a a^\dagger a + \omega_b b^\dagger b + \omega_c c^\dagger c$, the Hamiltonian is obtained as

$$
\begin{aligned}
H_S(t) = {} & S_a(t) a^\dagger a + S_b(t) b^\dagger b + \chi_a a^{2\dagger} a^2 + \chi_b b^{2\dagger} b^2 \\
& + \chi_{ab} a^\dagger a b^\dagger b - i g_{swap}(t)(b^\dagger a - a^\dagger b), \quad (10)
\end{aligned}
$$

where the parameters are as follows:

$$
\chi_{a(b)} = \frac{-2\pi^4 E_J \cos\left(\frac{\varphi_{dc}}{2}\right)}{\phi_0^4} \lambda_{a(b)}^4,
$$

$$
\chi_{ab} = \frac{-8\pi^4 E_J \cos\left(\frac{\varphi_{dc}}{2}\right)}{\phi_0^4} \lambda_a^2 \lambda_b^2,
$$

$$
g_{swap}(t) = \left(\frac{\pi^2}{\phi_0^2} - \frac{\bar\lambda \pi^4}{\phi_0^4}\right) E_J \sin\left(\frac{\varphi_{dc}}{2}\right) \lambda_a \lambda_b F(t),
$$

$$
S_{a(b)}(t) = \left(\frac{\bar\lambda \pi^4}{\phi_0^4} - \frac{\pi^2}{\phi_0^2}\right) \frac{E_J \cos\left(\frac{\varphi_{dc}}{2}\right) \lambda_{a(b)}^2}{4} F(t)^2, \quad (11)
$$

and $S_{a(b)}(t)$ are the Stark shifts induced by the flux drive. The dressed mode coefficients $\lambda_{a(b)}$ in Eqs. (7) and (11) are proportional to the ratio $\lambda_{a(b)} \propto g_{a(b),c}/\Delta_{a(b),c}$, where $g_{a(b),c}$ and $\Delta_{a(b),c}$ correspond to the coupling strength and detuning between the coupler and the storage (leakage) cavity. The coupler is coupled to the storage (leakage) cavities through the coupling capacitance C_{ac} (C_{bc}), where by changing the capacitance strengths different values of the conversion rates g_{swap} and also nonlinear terms χ_{ab}, $\chi_{a(b)}$ will be obtained; see Fig. 3. As shown in Fig. 3, the reduction (increase) of the non-linearities $\chi_{a(b)} \propto \lambda_{a(b)}^4$ yields a similar effect on the swap rate $g_{swap}(t) \propto \lambda_a \lambda_b$; as mentioned, $\lambda_{a(b)} \propto g_{a(b),c} \propto C_{a(b)c}$. It is worth noting that a higher amplitude of the drive $F(t)$ makes a stronger swap rate $g_{swap}(t)$ and accelerates the transfer and release process, but in this regime the Hamiltonian of the system acquires higher-order nonlinear interactions.

The leakage cavity is coupled to the waveguide and decays with a constant rate κ. The analysis of the emitted radiation is equivalent to the one presented for the toy model in Sec. II,
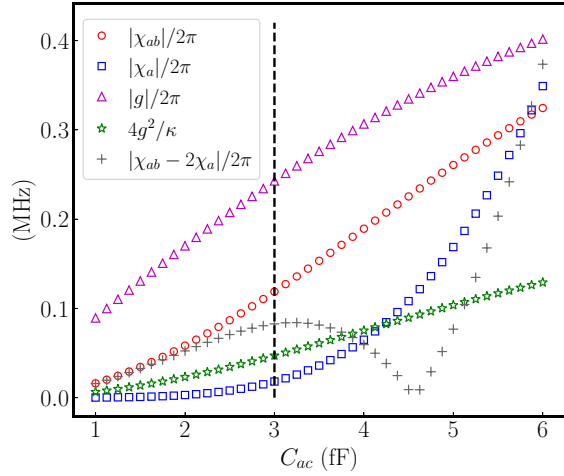
FIG. 3. The change of the nonlinear parameters χ_a, χ_{ab}, swap rate g, detuning from resonant interaction $\chi_{ab} - 2\chi_a$, and Purcell rate $4g^2/\kappa$ as functions of the value of the coupling capacitance C_{ac}, where $1/\kappa = 0.2\,\mu s$. The vertical black dashed line corresponds to the parameters used to simulate the lower panels in Fig. 4.

with the master equation,

$$\frac{\partial \varrho(t)}{\partial t} = -i[H_S(t), \varrho(t)] + \kappa\left(b\varrho(t)b^\dagger - \frac{1}{2}\{b^\dagger b, \varrho(t)\}\right), \quad (12)$$

where $H_S(t)$ is given in Eq. (10), and the Lindblad operator $\sqrt{\kappa}b$ describes the dissipation of the leakage cavity to the waveguide. As for the toy model in Eq. (4), the mode decomposition of the first-order correlation function of the field operator $\sqrt{\kappa}b$ determines the most populated orthonormal output modes.

As we saw in Sec. II, nonlinear terms in the Hamiltonian cause the output field to populate several temporal field modes of the waveguide. Since the self-Kerr and cross-Kerr terms ($\chi_a a^{\dagger 2} a^2$, $\chi_b b^{\dagger 2} b^2$ and $\chi_{ab} a^\dagger b^\dagger ab$) are inevitable consequences of the tunable coupling in our system, the output field will indeed populate many temporal modes, as will be seen in the next section.

In the limit where κ is much larger than the other couplings in the master equation, it is possible to adiabatically eliminate the leakage cavity and obtain an effective Markovian master equation for the storage cavity mode with a Purcell damping rate $\simeq 4g_{\text{swap}}^2/\kappa$; green dots in Fig 3. While we do not rely on the quantitative validity of this effective treatment in our numerical studies, we will refer to the value of the Purcell rate in the analysis of the results.

Here, we also note that, due to the presence of other dissipation channels, the release process cannot be made arbitrarily slow. Hence, in the experiment, there will be a tradeoff between the loss to many less populated modes in the rapid-release regime and to other dissipation channels in the slow-release regime.

IV. RELEASE OF FOCK STATES AND CAT STATES

As illustrated in Sec. II, a linear resonator emits any initial quantum state into a single spatiotemporal mode determined by the time-dependent out-coupling strength. However, the temporal shape of the output field from a nonlinear emitter is correlated with the photon number contents. In this section, we expand such analysis to investigate how the multimode character of the output field of the emitter in Fig. 2 is affected by different values of the coupling strength between the coupler and the storage cavity. As discussed in the preceding section, the coupling capacitance C_{ac} controls both the coherent swap strengths between the cavities, the cavity nonlinearities, and the effective Purcell decay rate of the storage cavity, as shown in Fig. 3.

In Fig. 4, we investigate the output field of the emitter for the release of different quantum states such as a Fock state (FS) $|\psi\rangle = |n\rangle$, a two-component cat state (TCCS)

$$|\psi\rangle \propto |\alpha\rangle + |-\alpha\rangle \propto \sum_{n=0}^{\infty} \frac{\alpha^{2n}}{\sqrt{(2n)!}} |2n\rangle, \quad (13)$$

which is a promising candidate for correcting dephasing errors [33,34], and a four-component cat state (FCCS)

$$|\psi\rangle \propto |\alpha\rangle + |-\alpha\rangle + |i\alpha\rangle + |-i\alpha\rangle \propto \sum_{n=0}^{\infty} \frac{\alpha^{4n}}{\sqrt{(4n)!}} |4n\rangle, \quad (14)$$

which can be used for quantum storage and communication in the presence of photon loss [35,36].

Figure 4(a) shows the relative population of the most populated mode n_1/n_{out} as a function of the Kerr nonlinearities. The ratio n_1/n_{out} reveals the multimode character of the output field released from a three-photon FS and TCCS and FCCS, composed of coherent states with amplitude $\alpha = \sqrt{3}$. As one expects, the output field becomes more multimode with higher values of nonlinearity. Figure 4(b) shows n_1/n_{out} as a function of the initial mean photon number of the storage cavity for the same states using fixed nonlinear parameters, corresponding to the dashed vertical line in Fig. 3. As expected, with a higher number of photons, the resonator nonlinearity leads to an output field occupying more modes.

We observe that the FS and the FCCS yield a higher single-mode content than the TCCS with the same photon number. This difference arises because the FCCS and TCCS populate the Fock components $|0\rangle + |4\rangle$ and $|0\rangle + |2\rangle + |4\rangle$, respectively. Since the Fock component $|0\rangle$ represents a vacuum state in all modes, and hence also the modes occupied by the release of $|4\rangle$, we retain a superposition of zero and four photons in the most populated mode, while the two Fock components $|2\rangle$, $|4\rangle$ of the TCCS may populate very different modes and hence not produce the TCCS in any single output mode.

In Fig. 4, panel (a), the output field is almost single mode, $n_1/n_{\text{out}} \simeq 1$, until $\chi_{ab}/2\pi$ exceeds the value -0.23 MHz or equivalently the value $C_{ac} \simeq 4.5$ fF in Fig. 3. This can be ascribed to the release process of each photon from storage cavity to the leakage cavity and then to the waveguide. For each Fock component $|n\rangle_a$ of the storage cavity, the transformation of a photon to the leakage cavity is mediated by the beam splitter interaction process, $|n, 0\rangle_{a,b} \xrightarrow{\text{beam splitter}} |n-1, 1\rangle_{a,b}$, where, consequently by decaying to the waveguide $|n-1, 1\rangle_{a,b} \xrightarrow{\text{decay to waveguide}} |n-1, 0\rangle_{a,b}$, the photon is
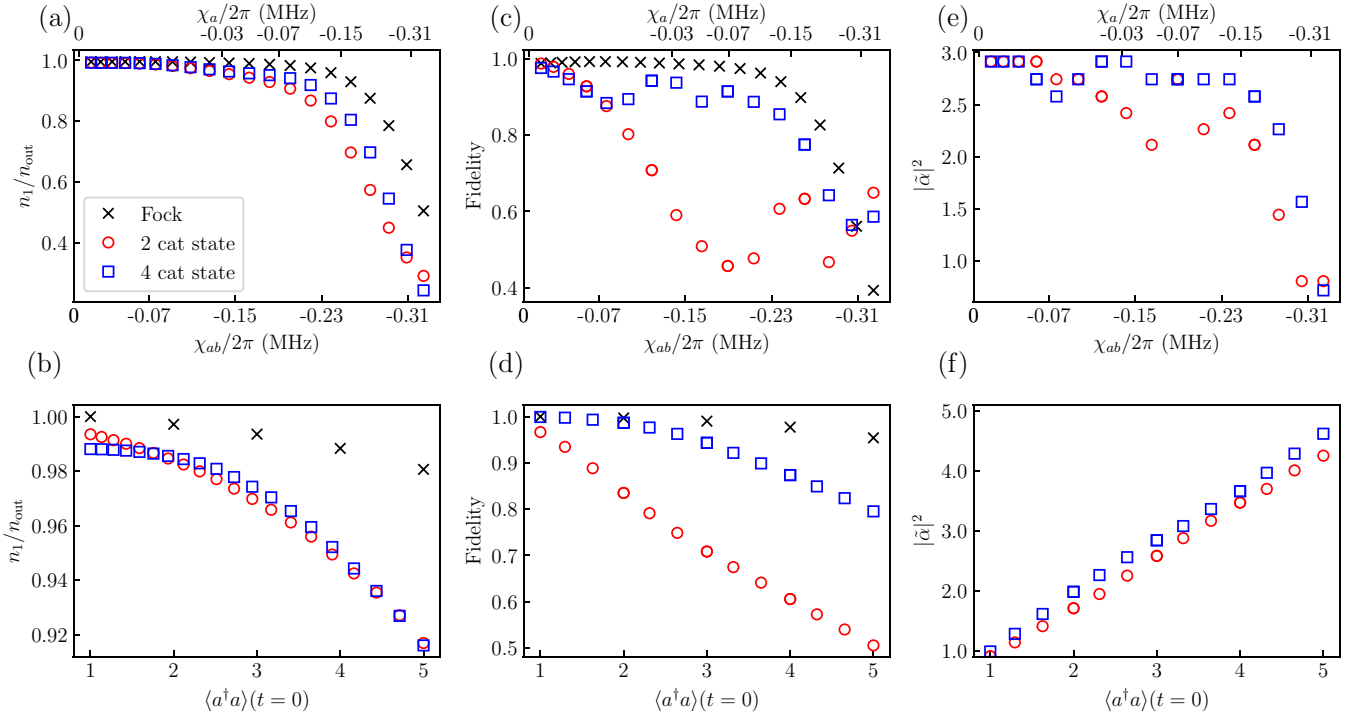
FIG. 4. The characteristics of the output field for different initial quantum states such as a FS $|n\rangle$, a TCCS (13), and a FCCS (14). The upper panels show (a) the relative occupation of the most populated mode, (c) the state fidelity of the state occupying that mode with respect to the optimal target state, see Eq. (17), and (e) the value of the cat state amplitude $\tilde{\alpha}$ that has the maximum fidelity with the state occupying the most populated mode. The results are shown for the initial FS $|n = 3\rangle$ and FCCS and TCCS with amplitude parameter $\alpha = \sqrt{3}$. They are calculated as a function of the nonlinear coupling strengths χ_{ab} and χ_a indicated along the lower and upper axes, which in turn correspond to a varying capacitance between the storage cavity and the coupler in the physical system (see Fig. 3). The self-Kerr χ_b is not specified as the leakage cavity is mostly occupied by the vacuum and the occasional one-photon state. In the lower panels, we assume nonlinear interaction parameters $\chi_{ab}/2\pi = -0.11$ MHz, $\chi_a/2\pi = -0.017$ MHz, and $\chi_b/2\pi = -0.04$ MHz, and we show the same quantities as in the upper panels but for different values of the initial mean photon number $\langle a^\dagger a\rangle(t = 0)$; see Sec. V for details.

released. It is worth noting that, due to the large decay rate κ the population of Fock components $n \geqslant 2$ of the leakage cavity is suppressed. The energy difference between the states $|n, 0\rangle_{a,b}, |n - 1, 1\rangle_{a,b}$ is $\Delta E_n = (n - 1)(2\chi_a - \chi_{ab})$, where a small additional shift is omitted; see Eq. (10). If $\chi_{ab} \simeq 2\chi_a$, the transfer is resonant and faster, which results in a more single-mode character. According to Fig. 3, the energy difference ΔE_n is limited until $C_{ac} \simeq 4.5$ fF, and thereafter it rapidly increases and the transition of a photon between the states becomes nonresonant and slow, which in combination with the nonlinearity causes the increasing multimode character, witnessed by the reduction of the population n_1/n_{out} and similar reductions in the other quantifiers of the output field.

V. CHARACTERIZING THE MOST POPULATED MODE

In order to investigate how well the initial state of the storage cavity is transferred to the waveguide, the quantum state of the output modes needs to be considered. This section addresses the quantum state contents of the most occupied mode v_1. This is done by the formalism introduced in [24], which, for the theoretical calculation assumes a downstream ideal linear cavity with mode operators $d, d^\dagger$, coupled to the

system by the interaction Hamiltonian

$$H_{b,v_1}(t) = \frac{i\sqrt{\kappa}}{2}[g_{v_1}^*(t)b^\dagger d - g_{v_1}(t)d^\dagger b]. \quad (15)$$

The time-dependent coupling between the cavity and waveguide,

$$g_v(t) = -\frac{v_1^*(t)}{\sqrt{\int_0^t dt' |v_1(t')|^2}}, \quad (16)$$

ensures that the cavity captures the contents of the temporal mode $v_1(t)$. The dynamics of the cascaded system is described by the Lindblad master equation with total Hamiltonian $H_T = H_S(t) + H_{b,v_1}(t)$ and a single Lindblad operator describes dissipation to the waveguide, $L_0(t) = \sqrt{\kappa}b + g_{v_1}^*(t)d$, representing the interference between the emitted field of the leakage cavity and the ideal downstream cavity. This form of the master equation ensures the cascaded nature of the propagation of the fields, [37,38]. Here, we stress that the capturing cavity is a theoretical tool for analyzing the mode content of the field. For an experimental realization of the capturing cavity, we would encounter the same issues with nonlinearity as for the emission process.
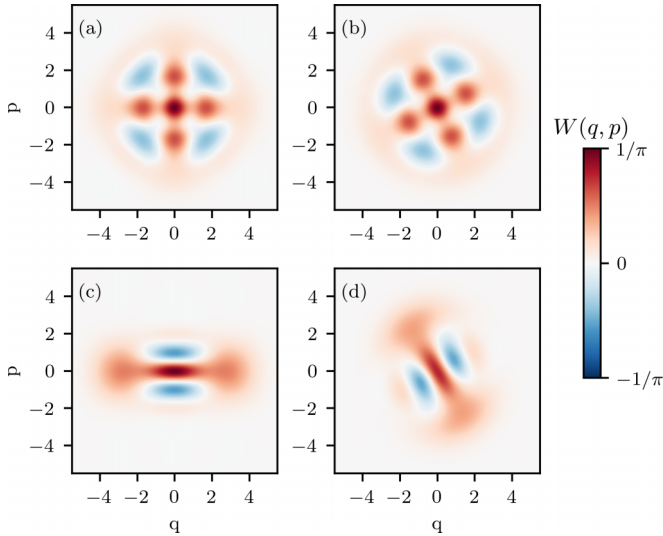
FIG. 5. Wigner function of the initial FCCS (a), TCCS (c), and of the state of the most populated modes of emission in the two respective cases (b,d). The amplitude of the initial cat states is $|\alpha| = \sqrt{2}$ and the nonlinear interactions are $\chi_{ab}/2\pi = -0.19\,\mathrm{MHz}$, $\chi_a/2\pi = -0.065\,\mathrm{MHz}$, and $\chi_b/2\pi = -0.034\,\mathrm{MHz}$. The amplitude of the single mode output FCCS that most resembles the state in panel (b) has $|\tilde{\alpha}| = \sqrt{1.96}$ with a corresponding fidelity $\mathcal{F}_{4\mathrm{cat}} = .97$. The state shown in panel (d) has a fidelity $\mathcal{F}_{2\mathrm{cat}} = 0.85$ with the TCCS with amplitude $|\tilde{\alpha}| = \sqrt{1.66}$ and it is obtained with the optimal rate t_0 and the fixed amplitude δ for the flux drive $F(t) = \delta \tanh(t/t_0)$; see Sec. V A for more explanation.

In the three oscillator description (a, b, d), the ideal state transformation is $|\psi, 0, 0\rangle_{a,b,d} \rightarrow |0, 0, \psi\rangle_{a,b,d}$. While the a and b oscillators may, indeed, be emptied with certainty, cavity d, will, in general, be occupied by a mixed state ϱ_d, as it is correlated with other modes of the output field.

Because the output field is not a single mode, the number of photons in the most populated output mode υ_1 is less than the initial number of photons in the storage cavity. As shown in Figs. 5(b) and 5(d), the output state in that mode may still be a catlike state $|\tilde{\psi}\rangle$, but with a modified amplitude $\tilde{\alpha}$. We thus vary the parameter $\tilde{\alpha}$ in order to maximize the fidelity

$$\mathcal{F} = \langle \tilde{\psi} | \varrho_d(T) | \tilde{\psi} \rangle, \tag{17}$$

over TCCS and FCCS cat states $|\tilde{\psi}\rangle$, where T is a time well after the emission of the temporal mode $\upsilon_1(t)$. For the Fock state fidelities, we calculate the population of the same Fock state $|\tilde{\psi}\rangle = |\psi\rangle$ as the initial state of the storage cavity.

Figure 4(c) shows the fidelity $\mathcal{F}$ of the quantum state occupying the most populated mode υ_1 as a function of the Kerr nonlinearities. For all three initial states, the fidelity is higher in the low Kerr regime; however, the fidelity of TCCS is affected more than the other quantum states, which we ascribe to the TCCS occupying more Fock components. In Fig. 4(c), in addition to the rapid reduction of the fidelity, a revival of the fidelity of the TCCS is observed in the higher nonlinear regime. This can be explained by considering the different phases θ_2 and θ_4 induced by the self-Kerr and cross-Kerr coefficients χ_a, χ_{ab} on the Fock components $|2\rangle$ and $|4\rangle$, respectively. For a certain amount of the nonlinearities, the

phases can be related by $\theta_4 \approx \theta_2 + 2\pi k$, recovering fidelity of the TCCS; see Fig. 8 in Appendix C for visualizations of the Wigner functions corresponding to Fig. 4(c).

Figures 4(e) and 4(f) show the size of the cat states with the highest fidelity $\tilde{\alpha}$ of the mode υ_1 as a function of the nonlinearities and the initial photon number, respectively. In Fig. 4(e), for both cat states, the amplitude $\tilde{\alpha}$ decreases with increasing nonlinearity as fewer photons populate the most populated mode; see Fig. 4(a). Figure 4(d) shows the fidelity of the FS, TCCS, and FCCS as functions of the initial mean photon number, where the higher photon numbers, as expected, yield more reduction in the fidelity.

In the low photon number regime, $n < 2$, the loss of photons to other modes is noticeable [Fig. 4(b)], but is not dominating over the reduction of the fidelity coming from the Kerr rotation. In the recent experiment [17], transferring TCCS and FCCS between a sender and a receiver, the dynamics is determined by a Hamiltonian similar to Eq. (10). In the supplementary material of [17], the fidelity reduction due to an effective Kerr rotation combined with photon loss is discussed. Our formalism gives a very similar picture, where we can quantify the cavity dephasing due to the population of multiple output modes. We find a 1% reduction of the population of the most populated output mode, which agrees with the analysis in [17].

A. Optimal drive to encode cat states into the most populated mode

As discussed in the previous section, the Kerr rotations affect the FCCS less, as only two Fock components $|0\rangle$, $|4\rangle$ are essentially populated and the effect can to a large extent be described by an effective phase acquired by $|4\rangle$. One realization of the initial and the released FCCS is shown in Fig. 5, panels (a) and (b), respectively. The initial amplitude is $|\alpha| = \sqrt{2}$ and the most occupied emitted mode has the highest fidelity with a FCCS with amplitude $|\tilde{\alpha}| = \sqrt{1.96}$ and the fidelity of $\mathcal{F}_{4\mathrm{cat}} = 0.97$, with the same drive shape and parameters $F(t) = \delta \tanh(t/t_0)$, as employed in Fig. 4.

In contrast to FCCS, the TCCS has three main Fock components $|0\rangle$, $|2\rangle$, and $|4\rangle$, thus involving two different effective phases on $|2\rangle$ and $|4\rangle$, which in general cannot be modeled by a single rotation of the Wigner function. To improve the fidelity for a specific set of nonlinear parameters, we optimize the flux drive on the coupler to minimize the effect of the nonlinear rotations and find an approximate TCCS with relation $\theta_4 \approx \theta_2 + 2\pi k$ and amplitude $|\tilde{\alpha}| < |\alpha|$. To this end, according to the drive shape $F(t) = \delta \tanh(t/t_0)$, we consider a fixed drive amplitude for parameter δ in the weak drive regime and we optimize the other variable, which is t_0, the rate of turning on the drive. We have optimized the drive according to the condition $\theta_4 \approx \theta_2 + 2\pi k$ to immunize the TCCS from nonlinear rotations and also large reduction in the fidelity. Figure 5(c) shows an initial TCCS with $|\alpha| = \sqrt{2}$, and Fig. 5(d) shows the state released in the most occupied mode using the optimal drive rate $t_0 = 7.3$ μs, which is almost 5 times slower than the one employed for Figs. 4, 5(a), and 5(b). A TCCS with amplitude $|\tilde{\alpha}| = \sqrt{1.66}$ (up to a linear rotation) shows the largest fidelity $\mathcal{F}_{2\mathrm{cat}} = 0.85$ with the state illustrated in Fig. 5(d).

VI. SUMMARY

We studied the characteristics of the quantum state released from a realistic nonlinear emitter. To optimally release the desired quantum states into a propagating mode, we utilized a flux-tunable coupler to transfer the quantum state from the storage cavity to the waveguide. We have shown, that due to the nonlinear interactions in the emitter, the output field obtains a multimode character, where the shape of the modes and their photon population become correlated. We investigated the output field for Fock states and two- and four-component cat states. We also studied the adjustment of the flux drive to emit an optimal cat state into the most populated mode. Our results showed that in the low photon number regime the fidelity reduction due to the nonlinear interactions is clearly noticeable (on the percent level), but it is not the dominant contribution to the experimentally observed reduction in fidelity, seen in recent experiments [16,17].

Our calculation and simulation results illustrate a tradeoff between the speed of emission and the effective nonlinearities of the emitter. This may suggest that using more elaborate couplers with more tunability, e.g., a superconducting nonlinear asymmetric inductive element (SNAIL) based coupler [39], may improve the fidelity of the beam-splitter gate $\propto H_{bs}(t)$ [40]. However, according to our formalism, in aiming for high-fidelity state transfer of multiphoton states, the multimode aspects of the transmitted field are unavoidable and need to be taken into account.

Lastly, it is worthwhile to note that, to actually catch a single mode using a linear receiver, it is enough to use the time-inverted drive compared to the one used in a linear transmitter [41]. A realistic nonlinear emitter, however, generates a multimode output field, and we would need a nonlinear receiver to optimally reabsorb the output field. The concept of time reversal can be used as a guiding principle, but how to find such a receiver in practice is still an open question.

ACKNOWLEDGMENTS

APPENDIX A: LAGRANGIAN OF THE QUANTUM CIRCUIT OF THE EMITTER

The quantum circuit of Fig. 2 is shown in detail in Fig. 6. We consider the two cavities as lumped elements including capacitances $C_{a(b)}$ in parallel with the inductances $L_{a(b)}$. The coupler is described by the total capacitance C_c, junction energy E_j, and the AC flux drive $\varphi_{\text{ext}}(t)$. The coupler capacitively is coupled to the storage and leakage cavity through the capacitances C_{ac}, C_{bc}, respectively. The capacitance C_{bL} is the coupling between the leakage cavity and the transmission line, which gives rise to a minor frequency shift of the leakage cavity. The red dots show the flux of each system with which the Lagrangian and the Hamiltonian of the system can be evaluated.
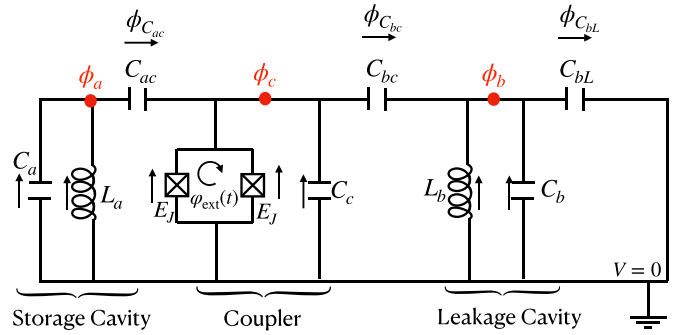

FIG. 6. Quantum circuit of the emitter. The coupler is derived to properly transfer a quantum state from storage to the leakage cavity. Both cavities are shown by lumped elements which capacitively are coupled to a symmetry flux tunable transmon.

To properly drive the effective Hamiltonian we first evaluate the lagrangian of the quantum circuit $\mathcal{L} = \mathcal{T} - \mathcal{V}$ where $\mathcal{T}$ and $\mathcal{V}$ correspond to the kinetic and potential energy, respectively.

According to Fig. 6, the kinetic energy is evaluated as

$$\mathcal{T} = \tfrac{1}{2}\big[C_a\dot{\phi}_a^2 + C_{ac}\dot{\phi}_{C_{ac}}^2 + C_c\dot{\phi}_c^2 + C_{bc}\dot{\phi}_{C_{bc}}^2 + C_b\dot{\phi}_b^2 + C_{bL}\dot{\phi}_{C_{bL}}^2\big] \tag{A1}$$

and the potential is

$$\mathcal{V} = \frac{1}{2}\left[\frac{\phi_a^2}{L_a} + \frac{\phi_b^2}{L_b}\right] - 2E_J \cos\left(\frac{\pi\phi_{\text{ext}}(t)}{\phi_0}\right)\cos\left(\frac{2\pi\phi_c}{\phi_0}\right), \tag{A2}$$

where the detail of the derivation of the coupler potential is provided in Appendix B. Using Kirchoff's voltage laws

$$\dot{\phi}_{C_{ac}} = \dot{\phi}_c - \dot{\phi}_a, \quad \dot{\phi}_{C_{bc}} = \dot{\phi}_b - \dot{\phi}_c, \quad \dot{\phi}_{C_{bL}} = -\dot{\phi}_b, \tag{A3}$$

and the conjugate relation

$$Q_i = \frac{\partial\mathcal{L}}{\partial\dot{\phi}_i}, \qquad i = a, c, b, \tag{A4}$$

the kinetic energy in the charge basis $[Q_a, Q_c, Q_b]$ is obtained as

$$\mathcal{T} = \frac{1}{2}\vec{Q}\mathcal{C}\vec{Q}^T, \tag{A5}$$

where

$$\mathcal{C} \approx \begin{bmatrix} \frac{1}{\mathbf{C_a}} & \frac{C_{ac}}{\mathbf{C_a}\mathbf{C_c}} & 0 \\[2mm] \frac{C_{ac}}{\mathbf{C_a}\mathbf{C_c}} & \frac{1}{\mathbf{C_c}} & \frac{C_{bc}}{\mathbf{C_b}\mathbf{C_c}} \\[2mm] 0 & \frac{C_{bc}}{\mathbf{C_b}\mathbf{C_c}} & \frac{1}{\mathbf{C_b}} \end{bmatrix}. \tag{A6}$$

In the capacity matrix, $\mathbf{C_a} = C_a + C_{ac}$, $\mathbf{C_c} = C_c + C_{bc} + C_{ac}$, $\mathbf{C_b} = C_b + C_{bc} + C_{bL}$. According to the capacitance matrix, the coupling strength between the coupler and the storage(leakage) cavity depends on $g_{ac} \propto \frac{C_{ac}}{\mathbf{C_a}\mathbf{C_c}}$, $g_{bc} \propto \frac{C_{bc}}{\mathbf{C_b}\mathbf{C_c}}$, respectively, where we assume the coupling is weak, $C_{ac}, C_{bc} \ll C_a, C_b, C_c$.

1. Linear and nonlinear potential of the coupler

From Eq. (A2), the potential energy of the coupler includes the contribution of the nonlinear flux operators and the external drive as

$$U_{\text{coupler}} = -2E_J \cos\left(\frac{\pi\phi_{\text{ext}}}{\phi_0}\right) \cos\left(\frac{2\pi\phi_c}{\phi_0}\right)$$

$$= -2E_J \cos\left(\frac{\varphi_{\text{ext}}(t)}{2}\right) \cos(\varphi_c), \qquad \text{(A7)}$$

where the reduced flux is considered as $\varphi_c = \frac{2\pi\phi_c}{\phi_0}$ and $\varphi_{\text{ext}}(t) = \varphi_{\text{dc}} + F(t)\sin(\omega_d t)$. Using the Taylor expansion

$$\cos(\varphi_c) = 1 - \frac{\varphi_c^2}{2} + \frac{\varphi_c^4}{4!} + \mathcal{O}(\varphi_c^6), \qquad \text{(A8)}$$

the potential energy of the transmon can be decomposed into a linear U_C^l and nonlinear U_C^{nl} terms as (the constant terms are dropped)

$$U_{\text{coupler}} = U_C^l + U_C^{nl},$$

$$U_C^l = -2E_J \cos\left(\frac{\varphi_{\text{ext}}(t)}{2}\right)\left[1 - \frac{\varphi_c^2}{2}\right],$$

$$U_C^{nl} = -2E_J \cos\left(\frac{\varphi_{\text{ext}}(t)}{2}\right)\left[\frac{\varphi_c^4}{4!}\right]. \qquad \text{(A9)}$$

By expanding the flux drive term

$$\cos\left(\frac{\varphi_{\text{ext}}(t)}{2}\right) = \cos\left(\frac{\varphi_{\text{dc}}}{2}\right) - \frac{\sin\left(\frac{\varphi_{\text{dc}}}{2}\right)F(t)\sin(\omega_d t)}{2}$$

$$- \frac{\cos\left(\frac{\varphi_{\text{dc}}}{2}\right)}{8}F(t)^2 \sin(\omega_d t)^2 + \mathcal{O}(F(t)^3), \qquad \text{(A10)}$$

the quadratic part of the potential, second line of (A9), can be decomposed into time-independent and time-dependent terms as

$$U_C^l = E_J\left[\cos\left(\frac{\varphi_{\text{dc}}}{2}\right)\right]\varphi_c^2 - E_J\left[\frac{\sin\left(\frac{\varphi_{\text{dc}}}{2}\right)F(t)\sin(\omega_d t)}{2}\right.$$

$$\left. + \frac{\cos\left(\frac{\varphi_{\text{dc}}}{2}\right)}{8}F(t)^2 \sin(\omega_d t)^2\right]\varphi_c^2. \qquad \text{(A11)}$$

Consequently one can easily find the time-independent potential matrix $\mathcal{V}'$ in basis $\phi = (\phi_a, \phi_c, \phi_b)x$:

$$\mathcal{V}' = \begin{bmatrix} \frac{1}{L_A} & 0 & 0 \\ 0 & \frac{8\pi^2 E_J\left[\cos\left(\frac{\varphi_{\text{dc}}}{2}\right)\right]}{\phi_0^2} & 0 \\ 0 & 0 & \frac{1}{L_B} \end{bmatrix}, \qquad \text{(A12)}$$

which makes the potential energy $\mathcal{V} = \frac{1}{2}\vec{\phi}\mathcal{V}'\vec{\phi}^T$. Using the linear potential $\mathcal{V}$ and the kinetic energy $\mathcal{T}$, the dressed mode of the circuit can be evaluated. In the dressed mode, the time-dependent and nonlinear terms of the potential of the coupler provide the value of the effective nonlinear interaction on the cavities and the optimal swap operator between the cavities, which are discussed in the next section.

2. Dressed modes and the effective Hamiltonian

To calculate the dressed mode of the circuit in Fig. 6, one can define the linear and time-independent Hamiltonian as

$$H^l = \tfrac{1}{2}\vec{Q}\mathcal{C}\vec{Q}^T + \tfrac{1}{2}\vec{\phi}\mathcal{V}'\vec{\phi}^T, \qquad \text{(A13)}$$

where $\mathcal{C}, \mathcal{V}'$ are evaluated in Eqs. (A6) and (A12), respectively. The equation of motion for the Heisenberg operator is given by

$$\partial_t^2\vec{Q}^T = -\mathcal{V}'\mathcal{C}\vec{Q}^T,$$

$$\partial_t^2\vec{\phi}^T = -\mathcal{C}\mathcal{V}'\vec{\phi}^T, \qquad \text{(A14)}$$

and can be solved by making the ansatz

$$\vec{Q}^T = i\sum_n \sqrt{\frac{\hbar\omega_n}{2}}\frac{1}{\sqrt{\mathcal{C}}}\vec{\zeta}_n^T(a_n^\dagger e^{i\omega_n t} - a_n e^{-i\omega_n t})$$

$$\vec{\phi}^T = \sum_n \sqrt{\frac{\hbar}{2\omega_n}}\sqrt{\mathcal{C}}\vec{\zeta}_n^T(a_n^\dagger e^{i\omega_n t} + a_n e^{-i\omega_n t}). \qquad \text{(A15)}$$

The frequency of the modes ω_n and its corresponding orthogonal mode functions $\vec{\zeta}_n$ follow from the eigenvalue equation

$$\left(\sqrt{\mathcal{C}}\mathcal{V}'\sqrt{\mathcal{C}} - \omega_n^2 I\right)\vec{\zeta}_n^T = 0, \qquad \text{(A16)}$$

which yields the uncoupled Hamiltonian

$$H^l/h = \sum_{n=1}^3 \omega_n a_n^\dagger a_n. \qquad \text{(A17)}$$

The phase operator of the coupler ϕ_c, in the new basis a_i, can be expressed as

$$\phi_c = \sum_{n=1}^3 \frac{\lambda_n}{\sqrt{2}}(\hat{a}_n^\dagger + \hat{a}_n) = \sum_{n=1}^3 \frac{A_n + A_n^\dagger}{\sqrt{2}}$$

$$\longrightarrow \lambda_n = \sqrt{\frac{\hbar}{\omega_n}}\vec{e}_c\sqrt{\mathcal{C}}\vec{\zeta}_n^T, \qquad \text{(A18)}$$

where indices $i = 1, 2, 3$ correspond to a, c, b, respectively and we a introduce new parameters representation:

$$\lambda_a \equiv \lambda_1, \quad \lambda_c \equiv \lambda_2, \quad \lambda_b \equiv \lambda_3$$

$$a = a_1, \quad c = a_2, \quad b = a_3,$$

$$\omega_a = \omega_1, \quad \omega_c = \omega_2, \quad \omega_b = \omega_3. \qquad \text{(A19)}$$

Considering a compact form of the flux of the tunable coupler [31,32],

$$\phi_c = \frac{1}{\sqrt{2}}(A_a + A_a^\dagger + A_b + A_b^\dagger + A_c + A_c^\dagger) = \frac{A + A^\dagger}{\sqrt{2}}, \qquad \text{(A20)}$$

and defining $\bar{\lambda} = [A, A^\dagger] = |\lambda_a|^2 + |\lambda_b|^2 + |\lambda_c|^2$, the time-dependent part of Eq. (A11) is obtained as

$$H^l(t) = \frac{-2E_J\pi^2}{\phi_0^2}\left[\frac{\sin\left(\frac{\varphi_{\text{dc}}}{2}\right)F(t)\sin(\omega_d t)}{2}\right.$$

$$\left. + \frac{\cos\left(\frac{\varphi_{\text{dc}}}{2}\right)}{8}F(t)^2\sin(\omega_d t)^2\right](2A^\dagger A + \bar{\lambda}), \qquad \text{(A21)}$$

which provides the swap operator and the Stark shifts. In addition, the fourth order of the flux operator, U_C^{nl} in Eq. (A9), provides self-Kerr and cross-Kerr interaction, and also Stark shifts which in the dressed mode of Eq. (A20) are obtained as

$$U_C^{nl} = H_{nl} \approx \frac{-\pi^4 E_J \cos\left(\frac{\varphi_{\text{ext}}(t)}{2}\right)}{3\phi_0^4}(A + A^\dagger)^4$$

$$H_{nl} \approx \frac{-\pi^4 E_J \cos\left(\frac{\varphi_{\text{ext}}(t)}{2}\right)}{3\phi_0^4}[12\bar{\lambda}A^\dagger A + 6A^\dagger A^\dagger AA].$$
(A22)

It is worth noting that the dressed mode coefficients $\lambda_{a(b)} \approx g_{a(b),c}/(\omega_{a(b)} - \omega_c) \ll 1$, which allows us to neglect the contribution of the higher order nonlinearities in the effective Hamiltonian. In addition, we consider a weak drive which allows us to neglect higher order terms in the drive amplitude. However, in experiments it might be essential to go beyond this, e.g., see the calculations of the effective Hamiltonian in [42]. Furthermore, we have considered a flux driven coupler, but we note that also other coupling schemes qualitatively render similar effective Kerr terms [40]. If we consider the drive frequency $\omega_d = \omega_b - \omega_a$, the total Hamiltonian $H = $ (A17)+(A21)+(A22), in the rotating frame $\omega_a a^\dagger a + \omega_b b^\dagger b + \omega_c c^\dagger c$, is obtained:

$$H = -ig_{\text{swap}}(t)[b^\dagger a - a^\dagger b]$$
$$+ g_{\text{Stark}}(t)\left[\lambda_a^2 a^\dagger a + \lambda_b^2 b^\dagger b + \lambda_c^2 c^\dagger c\right]$$
$$+ g_{\text{selfKerr}}\left[\lambda_a^4 a^{2\dagger} a^2 + \lambda_b^4 b^{2\dagger} b^2 + \lambda_c^4 c^{2\dagger} c^2\right]$$
$$+ g_{\text{crossKerr}}\left[\lambda_a^2 \lambda_b^2 b^\dagger b a^\dagger a + \lambda_a^2 \lambda_c^2 c^\dagger c a^\dagger a + \lambda_c^2 \lambda_b^2 b^\dagger b c^\dagger c\right],$$
(A23)

where the coefficients are evaluated as

$$g_{\text{swap}}(t) = \left(\frac{\pi^2}{\phi_0^2} - \frac{\bar{\lambda}\pi^4}{\phi_0^4}\right)E_J \lambda_a \lambda_b \sin\left(\frac{\varphi_{\text{dc}}}{2}\right)F(t), \quad (A24)$$

$$g_{\text{Stark}}(t) = \left(\frac{\bar{\lambda}\pi^4}{\phi_0^4} - \frac{\pi^2}{\phi_0^2}\right)\frac{E_J \cos\left(\frac{\varphi_{\text{dc}}}{2}\right)}{4}F(t)^2, \quad (A25)$$

$$g_{\text{selfkerr}} = \frac{-2\pi^4 E_J \cos\left(\frac{\varphi_{\text{dc}}}{2}\right)}{\phi_0^4}, \quad (A26)$$

$$g_{\text{crosskerr}} = \frac{-8\pi^4 E_J \cos\left(\frac{\varphi_{\text{dc}}}{2}\right)}{\phi_0^4}. \quad (A27)$$

It is worth noting that because the coupler is initialized in the ground state, the Hamiltonian (A23), decouples the coupler from both cavities which means the terms $(c^\dagger c a^\dagger a, c^\dagger c b^\dagger b, c^{\dagger 2}c^2)$ vanish at all times. Comparing Eqs. (10) and (A23)–(A27), the following parameters are introduced

$$\chi_{a(b)} = \frac{-2\pi^4 E_J \cos\left(\frac{\varphi_{\text{dc}}}{2}\right)}{\phi_0^4}\lambda_{a(b)}^4,$$

$$\chi_{ab} = \frac{-8\pi^4 E_J \cos\left(\frac{\varphi_{\text{dc}}}{2}\right)}{\phi_0^4}\lambda_a^2 \lambda_b^2,$$

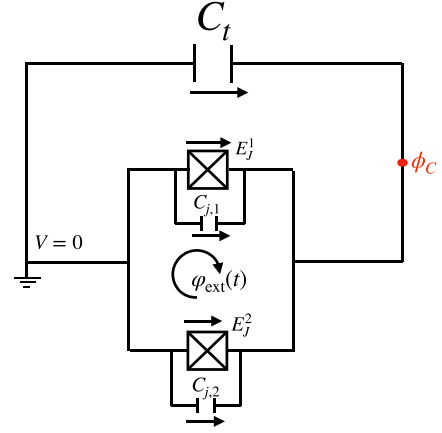$$S_{a(b)}(t) = g_{\text{Stark}}(t)\lambda_{a(b)}^2. \quad (A28)$$

FIG. 7. Schematic of a flux-tunable coupler. Two Josephson junction E_J^1, E_J^1 are in parallel with two parasitic (small) capacitance $C_{j,1}, C_{j,2}$ and shunted by a large capacitance C_t [30]. The flux drive in the small loop is $\varphi_{\text{ext}}(t)$ and the bigger loop is described by the flux operator ϕ_C.

APPENDIX B: CALCULATION OF THE POTENTIAL OF THE COUPLER

In general, we can consider each junction coupled in parallel with parasitic capacitance ($C_{j,1}, C_{j,2}$), and the total system is shunted by a large capacitance C_t; see Fig. 7. The Kinetic and potential energy of this simple circuit is

$$\mathcal{T} = \frac{1}{2}\left[C_t \dot{\phi}_C^2 + C_{j,1}\dot{\phi}_{j,1}^2 + C_{j,2}\dot{\phi}_{j,2}^2\right]$$

$$\mathcal{V} = -E_{J,1}\cos\left(\frac{2\pi\phi_{j,1}}{\phi_0}\right) - E_{J,2}\cos\left(\frac{2\pi\phi_{j,2}}{\phi_0}\right) \quad (B1)$$

According to the number of nodes in the circuit, it can be described by one degree of freedom which we consider ϕ_C. Using the Kirchhoff voltage low, the small loop of junctions obeys the following equation

$$\phi_{j,1} - \phi_{j,2} = \phi_{\text{ext}}. \quad (B2)$$

In the following, we introduce the independent parameter ϕ_C as the function of the two fluxes across the junctions

$$m_1\phi_{j,1} + m_2\phi_{j,2} = \phi_C \quad (B3)$$

Using Eq. ((B2),(B3)) the fluxes are obtained as

$$\phi_{j,1} = \frac{\phi_C + m_2\phi_{\text{ext}}}{m_1 + m_2}$$

$$\phi_{j,2} = \frac{\phi_C - m_1\phi_{\text{ext}}}{m_1 + m_2}, \quad (B4)$$

where subsequently, the kinetic part of Eq. (B1) can be rewritten as

$$\mathcal{T} = \frac{1}{2}\left[\left[\frac{C_{j,1} + C_{j,2}}{(m_1 + m_2)^2} + C_t\right]\dot{\phi}_C^2 + \frac{2(m_2 C_{j,1} - m_1 C_{j,2})}{(m_1 + m_2)^2}\dot{\phi}_C \dot{\phi}_{\text{ext}} + \mathcal{O}(\dot{\phi}_{\text{ext}})^2\right]. \quad (B5)$$
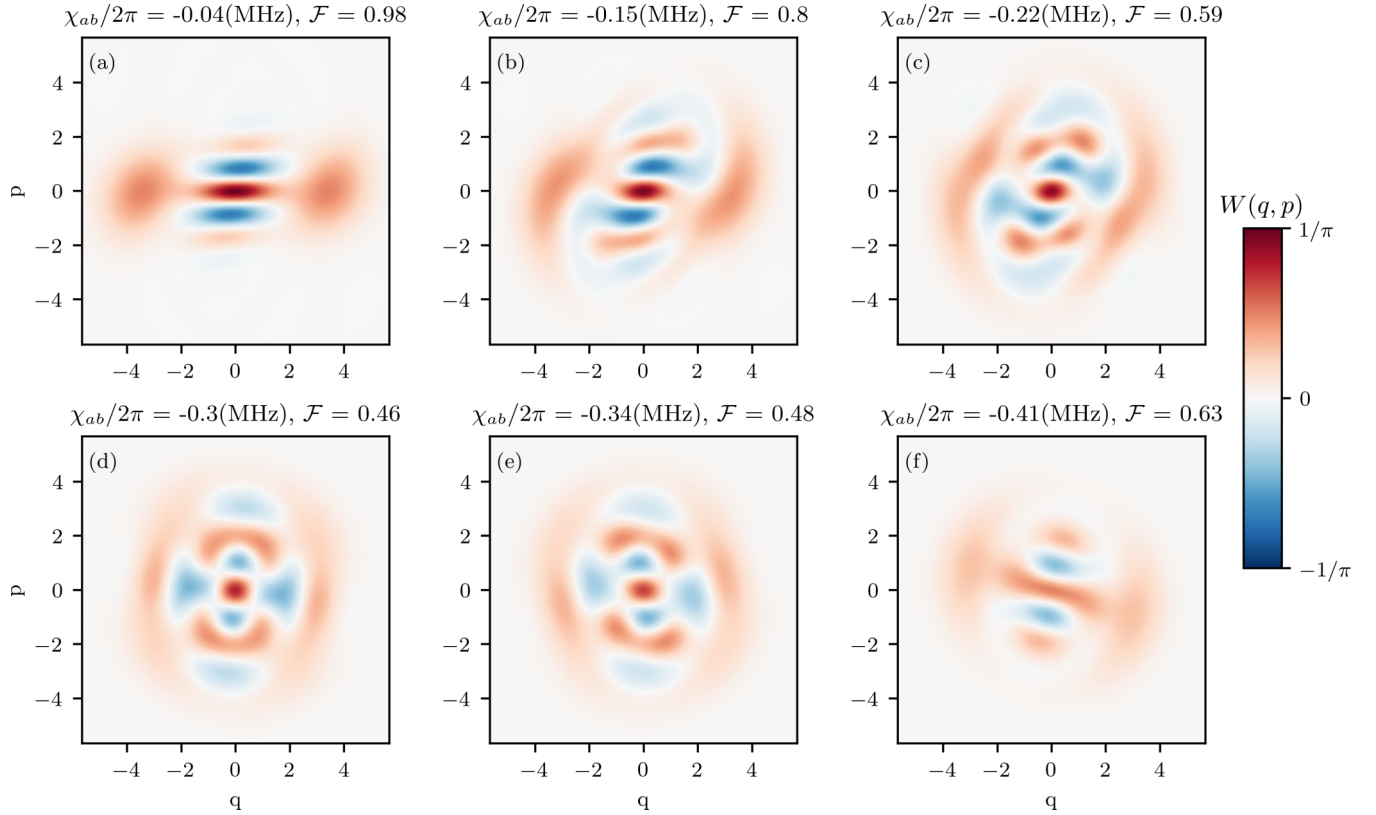
FIG. 8. Different realizations of the Wigner functions of the single output mode TCCS in Fig. 4(c).

We do not take the second order of the flux fluctuation into account, as we assume the flux drive is slow in time. To remove the effect of the flux drive fluctuation $\dot{\phi}_{\text{ext}}$, one can utilize the following two conditions

$$m_1 + m_2 = 1$$
$$m_2 C_{j,1} - m_1 C_{j,2} = 0, \tag{B6}$$

where lead to

$$m_1 = \frac{C_{j,1}}{C_{j,1} + C_{j,2}}$$
$$m_2 = \frac{C_{j,2}}{C_{j,1} + C_{j,2}}.$$

Hence $\mathcal{T}, \mathcal{V}$ are obtained as

$$\mathcal{T} = \frac{C_{j,1} + C_{j,2} + C_t}{2} \dot{\phi}_C^2$$
$$\mathcal{V} = -E_{J,1} \cos\left(\frac{2\pi[\phi_C + m_2\phi_{\text{ext}}]}{\phi_0}\right)$$
$$- E_{J,2} \cos\left(\frac{2\pi[\phi_C - m_1\phi_{\text{ext}}]}{\phi_0}\right). \tag{B7}$$

If we consider symmetry junction with $E_{J,1} = E_{J,2} = E_J$ and $C_{j,1} = C_{j,2}$, consequently $m_1 = m_2 = 1/2$ and the potential energy can be simplified as

$$\mathcal{V} = -2E_J \cos\left(\frac{2\pi\phi_C}{\phi_0}\right) \cos\left(\frac{\pi\phi_{\text{ext}}}{\phi_0}\right), \tag{B8}$$

which is equivalent to Eq. (A2). Introducing $C_c \equiv C_{j,1} + C_{j,2} + C_t$, the same kinetic energy as in Equation (A1) is obtained.

APPENDIX C: WIGNER FUNCTION OF FIG. 4(C)

Figure 8 shows different realizations of the Wigner function of the most populated output mode for TCCS shown in Fig. 4(c). As discussed in the main text, the nonlinear interactions have different effective phases on the Fock component $|2\rangle$, $|4\rangle$ which reduce the fidelity of the released TCCS into the most occupied mode.

[1] H. J. Kimble, The quantum internet, Nature (London) **453**, 1023 (2008).

[2] S. Wehner, D. Elkouss, and R. Hanson, Quantum internet: A vision for the road ahead, Science **362**, eaam9288 (2018).

[3] B. Vlastakis, G. Kirchmair, Z. Leghtas, S. E. Nigg, L. Frunzio, S. M. Girvin, M. Mirrahimi, M. H. Devoret, and R. J.

Schoelkopf, Deterministically encoding quantum information using 100-photon Schrödinger cat states, Science **342**, 607 (2013).

[4] Z. Leghtas, S. Touzard, I. M. Pop, A. Kou, B. Vlastakis, A. Petrenko, K. M. Sliwa, A. Narla, S. Shankar, M. J. Hatridge *et al.* Confining the state of light to a quantum

manifold by engineered two-photon loss, Science **347**, 853 (2015).

[5] N. Ofek, A. Petrenko, R. Heeres, P. Reinhold, Z. Leghtas, B. Vlastakis, Y. Liu, L. Frunzio, S. M. Girvin, L. Jiang *et al.*, Extending the lifetime of a quantum bit with error correction in superconducting circuits, Nature (London) **536**, 441 (2016).

[6] P. Campagne-Ibarcq, A. Eickbusch, S. Touzard, Evan Zalys-Geller, N. E. Frattini, V. V. Sivak, P. Reinhold, S. Puri, S. Shankar, R. J. Schoelkopf *et al.*, Quantum error correction of a qubit encoded in grid states of an oscillator, Nature (London) **584**, 368 (2020).

[7] S. Puri, L. St-Jean, J. A. Gross, A. Grimm, N. E. Frattini, P. S. Iyer, A. Krishna, S. Touzard, L. Jiang, A. Blais *et al.*, Bias-preserving gates with stabilized cat qubits, Sci. Adv. **6**, eaay5901 (2020).

[8] Z. Ni, S. Li, X. Deng, Y. Cai, L. Zhang, W. Wang, Z.-B. Yang, H. Yu, F. Yan, S. Liu *et al.*, Beating the break-even point with a discrete-variable-encoded logical qubit, Nature **616**, 56 (2023).

[9] A. L. Grimsmo, J. Combes, and B. Q. Baragiola, Quantum computing with rotation-symmetric bosonic codes, Phys. Rev. X **10**, 011058 (2020).

[10] D. Su, I. Dhand, and T. C. Ralph, Universal quantum computation with optical four-component cat qubits, Phys. Rev. A **106**, 042614 (2022).

[11] A. A. Houck, D. I. Schuster, J. M. Gambetta, J. A. Schreier, B. R. Johnson, J. M. Chow, L. Frunzio, J. Majer, M. H. Devoret, S. M. Girvin *et al.*, Generating single microwave photons in a circuit, Nature (London) **449**, 328 (2007).

[12] M. Pierre, I.-M. Svensson, S. R. Sathyamoorthy, G. Johansson, and P. Delsing, Storage and on-demand release of microwaves using superconducting resonators with tunable coupling, Appl. Phys. Lett. **104**, 232604 (2014).

[13] M. Pechal, L. Huthmacher, C. Eichler, S. Zeytinoğlu, A. A. Abdumalikov, S. Berger, A. Wallraff, and S. Filipp, Microwave-controlled generation of shaped single photons in circuit quantum electrodynamics, Phys. Rev. X **4**, 041010 (2014).

[14] S. R. Sathyamoorthy, A. Bengtsson, S. Bens, M. Simoen, Per Delsing, and G. Johansson, Simple, robust, and on-demand generation of single and correlated photons, Phys. Rev. A **93**, 063823 (2016).

[15] P. Forn-Díaz, C. W. Warren, C. W. S. Chang, A. M. Vadiraj, and C. M. Wilson, On-demand microwave generator of shaped single photons, Phys. Rev. Appl. **8**, 054015 (2017).

[16] W. Pfaff, C. J. Axline, L. D. Burkhart, U. Vool, Philip Reinhold, L. Frunzio, L. Jiang, M. H. Devoret, and R. J. Schoelkopf, Controlled release of multiphoton quantum states from a microwave cavity memory, Nat. Phys. **13**, 882 (2017).

[17] C. J. Axline, L. D. Burkhart, W. Pfaff, M. Zhang, Kevin Chou, P. Campagne-Ibarcq, P. Reinhold, L. Frunzio, S. M. Girvin, L. Jiang *et al.*, On-demand quantum state transfer and entanglement between remote microwave cavity memories, Nat. Phys. **14**, 705 (2018).

[18] D. Cozzolino, B. Da Lio, D. Bacco, and L. K. Oxenløwe, High-dimensional quantum communication: benefits, progress, and future challenges, Adv. Quantum Technol. **2**, 1900038 (2019).

[19] L. D. Burkhart, J. D. Teoh, Y. Zhang, C. J. Axline, L. Frunzio, M. H. Devoret, L. Jiang, S. M. Girvin, and R. J. Schoelkopf,

Error-detected state transfer and entanglement in a superconducting quantum network, PRX Quantum **2**, 030321 (2021).

[20] J. Yang, A. Eriksson, M. A. Aamir, I. Strandberg, C. C. Moreno, D. P. Lozano, P. Persson, and S. Gasparinetti, Deterministic generation of shaped single microwave photons using a parametrically driven coupler, arXiv:2303.02899.

[21] P. Krantz, M. Kjaergaard, F. Yan, T. P. Orlando, S. Gustavsson, and W. D. Oliver, A quantum engineer's guide to superconducting qubits, Appl. Phys. Rev. **6**, 021318 (2019).

[22] A. Blais, A. L Grimsmo, S. M. Girvin, and A. Wallraff, Circuit quantum electrodynamics, Rev. Mod. Phys. **93**, 025005 (2021).

[23] Y. Yin, Y. Chen, D. Sank, P. J. J. O'Malley, T. C. White, R. Barends, J. Kelly, E. Lucero, M. Mariantoni, A. Megrant, C. Neill, A. Vainsencher, J. Wenner, A. N. Korotkov, A. N. Cleland, J. M. Martinis, Catch and release of microwave photon states, Phys. Rev. Lett. **110**, 107001 (2013).

[24] A. H. Kiilerich and K. Mølmer, Input-output theory with quantum pulses, Phys. Rev. Lett. **123**, 123604 (2019).

[25] M. G. Raymer and I. A. Walmsley, Temporal modes in quantum optics: then and now, Phys. Scr. **95**, 064002 (2020).

[26] H.-P. Breuer, F. Petruccione *et al.*, *The Theory of Open Quantum Systems* (Oxford University Press, Oxford, 2002).

[27] C. Gardiner and P. Zoller, *Quantum Noise: A Handbook of Markovian and Non-Markovian Quantum Stochastic Methods with Applications to Quantum Optics* (Springer, New York, 2004).

[28] M. Tinkham, *Introduction to Superconductivity* (Dover, New York, 2004.

[29] J. Koch, Terri M. Yu, J. Gambetta, A. A. Houck, D. I. Schuster, J. Majer, A. Blais, M. H. Devoret, S. M. Girvin, and R. J. Schoelkopf, Charge-insensitive qubit design derived from the cooper pair box, Phys. Rev. A **76**, 042319 (2007).

[30] S. E. Rasmussen, K. S. Christensen, S. P. Pedersen, L. B. Kristensen, T. Bækkegaard, N. J. S. Loft, and N. T. Zinner, Superconducting circuit companion-an introduction with worked examples, PRX Quantum **2**, 040204 (2021).

[31] S. E. Nigg, H. Paik, B. Vlastakis, G. Kirchmair, S. Shankar, L. Frunzio, M. H. Devoret, R. J. Schoelkopf, and S. M. Girvin, Black-box superconducting circuit quantization, Phys. Rev. Lett. **108**, 240502 (2012).

[32] D. Marcos, P. Rabl, E. Rico, and P. Zoller, Superconducting circuits for quantum simulation of dynamical gauge fields, Phys. Rev. Lett. **111**, 110504 (2013).

[33] P. T. Cochrane, G. J. Milburn, and W. J. Munro, Macroscopically distinct quantum-superposition states as a bosonic code for amplitude damping, Phys. Rev. A **59**, 2631 (1999).

[34] A. P. Lund, T. C. Ralph, and H. L. Haselgrove, Fault-tolerant linear optical quantum computing with small-amplitude coherent states, Phys. Rev. Lett. **100**, 030503 (2008).

[35] Z. Leghtas, G. Kirchmair, B. Vlastakis, Robert J. Schoelkopf, Michel H. Devoret, and M. Mirrahimi, Hardware-efficient autonomous quantum memory protection, Phys. Rev. Lett. **111**, 120501 (2013).

[36] M. Mirrahimi, Z. Leghtas, V. V. Albert, S. Touzard, R. J. Schoelkopf, L. Jiang, and M. H. Devoret, Dynamically protected cat-qubits: A new paradigm for universal quantum computation, New J. Phys. **16**, 045014 (2014).

[37] H. J. Carmichael, Quantum trajectory theory for cascaded open systems, Phys. Rev. Lett. **70**, 2273 (1993).

[38] C. W. Gardiner, Driving a quantum system with the output field from another driven quantum system, Phys. Rev. Lett. **70**, 2269 (1993).

[39] N. E. Frattini, U. Vool, S. Shankar, A. Narla, K. M. Sliwa, and M. H. Devoret, 3-wave mixing Josephson dipole element, Appl. Phys. Lett. **110**, 222603 (2017).

[40] B. J. Chapman, S. J. de Graaf, S. H. Xue, Y. Zhang, James Teoh, J. C. Curtis, T. Tsunoda, A. Eickbusch, A. P. Read, A. Koottandavida, S. O. Mundhada, L. Frunzio, M. H. Devoret,

S. M. Girvin, and R. J. Schoelkopf, High-on-off-ratio beam-splitter interaction for gates on bosonically encoded qubits, PRX Quantum **4**, 020355 (2023).

[41] J. I. Cirac, P. Zoller, H. J. Kimble, and H. Mabuchi, Quantum state transfer and entanglement distribution among distant nodes in a quantum network, Phys. Rev. Lett. **78**, 3221 (1997).

[42] Y. Zhang, J. C. Curtis, C. S. Wang, R. J. Schoelkopf, and S. M. Girvin, Drive-induced nonlinearities of cavity modes coupled to a transmon ancilla, Phys. Rev. A **105**, 022423 (2022).